Initial observations of lunar impact melts and ejecta flows with the Mini-RF radar

Lynn M. Carter
NASA Goddard Space Flight Center
Planetary Geodynamics Lab, Code 698
Greenbelt, MD 20771

Catherine D. Neish, D. B. J. Bussey,
The Johns Hopkins University Applied Physics Lab
11100 Johns Hopkins Rd.
Laurel, MD 20723

Paul D. Spudis,
Lunar and Planetary Institute
3600 Bay Area Blvd.
Houston, TX 77058

G. Wesley Patterson, Joshua T. Cahill, R. Keith Raney
The Johns Hopkins University Applied Physics Lab
11100 Johns Hopkins Rd.
Laurel, MD 20723

Abstract: The Mini-RF radar on the Lunar Reconnaissance Orbiter spacecraft has revealed a great variety of crater ejecta flow and impact melt deposits, some of which were not observed in prior radar imaging. The craters Tycho and Glushko have long melt flows that exhibit variations in radar backscatter and circular polarization ratio along the flow. Comparison with optical imaging reveals that these changes are caused by features commonly seen in terrestrial lava flows, such as rafted plates, pressure ridges, and ponding. Small (<20 km) sized craters also show a large variety of features, including melt flows and ponds. Two craters have flow features that may be ejecta flows caused by entrained debris flowing across the surface rather than by melted rock. The circular polarization ratios (CPRs) of the impact melt flows are typically very high; even ponded areas have CPR values between 0.7-1.0. This high CPR suggests that deposits that appear smooth in optical imagery may be rough at centimeter- and decimeter- scales. In some places, ponds and flows are visible with no easily discernable source crater. These melt deposits may have come from oblique impacts that are capable of ejecting melted material farther downrange. They may also be associated with older, nearby craters that no longer have a radar-bright proximal ejecta blanket. The observed morphology of the lunar crater flows has implications for similar features observed on Venus. In particular, changes in backscatter along many of the ejecta flows are probably caused by features typical of lava flows.

1. Introduction

The impact process generates substantial melted material that is deposited in and around the crater. Early observations of the Moon revealed melt features associated with fresh impact craters; these features included thin veneers, ponds, and flows [*Shoemaker et al.,* 1968; Guest, 1973; *Howard and Wilshire*, 1975; *Hawke and Head*, 1977]. *Hawke and Head* [1977] found that the types and distribution of melt associated with impacts varies with crater size; craters with diameters less than 10 km were observed to have mostly veneers and small ponds on and outside the rims, while larger 20-50 km diameter craters are more likely to have significant melt flows. Ponds and melt flows can be found up to two crater radii from the rim of lunar craters, and the largest craters (above 50 km diameter) were observed to have ponds, but no flows [*Hawke and Head* 1977].

Magellan radar images of Venus also revealed long impact crater ejecta flows with complex radar backscatter variations that extend up to 14 crater radii from the rims [*Phillips et al.* 1991; *Chadwick and Schaber* 1993; *Asimov and Wood* 1992]. The transitions between radar bright and radar dark backscatter within a given flow have been attributed to various types of surface roughness changes, including differences in entrained clast abundance along the flow [*Chadwick and Schaber* 1993], deposition of rough, blocky material caused by topographic obstruction of a transient impact-induced hot vapor cloud [*Schultz* 1992], or changes in lava-like flow features that form in flowing impact melt [*Johnson and Baker*, 1994].

There are also multiple models for ejecta flow formation, which fall into two major categories. The first group of models suggests that the flows are caused by hot, turbulent density currents similar to pyroclastic flows that entrain melt, vapor and debris [*Shoemaker et*

65 *al.* 1986; *Phillips et al.* 1991; *Schultz et al.* 1992]. This flow emplacement mechanism is
66 sometimes suggested to be an early stage process, particularly because proximal crater ejecta
67 blanket materials often appear to overlie flow features on Venus [*Asimov and Wood* 1992]. In
68 this case, crater ejecta may have flow-like boundaries that are produced primarily by
69 deposition of solid debris rather than by flowing melted rock.
70 A second hypothesis suggests that, subsequent to ejecta emplacement, melted rock
71 undergoes late-stage segregation and then travels over the surface like a lava flow [*Shoemaker*
72 *et al.* 1968; *Phillips et al.* 1991; *Asimov and Wood* 1992; *Johnson and Baker* 1994]. In this
73 case, the flow boundaries are created by the impact melt, which likely entrains both country
74 rock and ejecta clasts as it flows over and around the previously emplaced ejecta. For the
75 Venus craters, it is possible that both processes (debris-rich flows and flowing impact melt)
76 can occur and this leads to the variety of different flow morphologies seen in radar images.
77 The prevalence and length of the ejecta flows on Venus are likely due to a combination of
78 factors, including the high surface temperatures, high mean impact velocities, and high
79 atmospheric pressure [*Phillips et al.* 1991; *Asimov and Wood* 1992].
80 There are multiple physical parameters that influence the emplacement of melted rock
81 during and after impacts. The angle of impact controls the direction of ejected material and
82 can lead to increased deposition of melt downrange and to the sides of the impact site [*Schultz*
83 1996; *Pierazzo and Melosh* 2000]. Impact angle is often cited as one of the primary
84 contributors to large amounts of melt deposition outside the crater [*Hawke and Head* 1977;
85 *Phillips et al.* 1991]. Melt flows will contain some component of unmelted country rock clasts
86 produced by the impact event, of which increasing amounts will increase the viscosity of the
87 flow. Topographic gradients can allow melt to escape from the crater walls, speed or slow the

88 flow as it travels across the surface, or trap melt material in topographic lows to form ponds
89 [*Hawke and Head* 1977; *Johnson and Baker* 1994]. Recent images from the Lunar
90 Reconnaissance Orbiter Camera (LROC) Narrow Angle Camera (NAC) have shown a
91 complex evolution of melt flows, including multiple-stage melt injection, flow inflation,
92 erosion of crater walls and uphill movement of melt [*Bray et al.* 2010]. These processes
93 suggest that the formation of melt flow features may vary extensively depending on the
94 impact conditions, and may have relatively long cooling times [*Bray et al.* 2010].
95 Radar observations of the lunar melt flows can provide additional information beyond
96 what can be learned with optical imaging. Radar is sensitive to roughness on the scale of the
97 radar wavelength, and at S-band wavelengths (12.6 cm), it can be used to assess surface and
98 sub-surface roughness of the centimeter to decimeter scale. This is somewhat smaller than
99 what is directly visible in high-resolution imaging, including the LROC NAC, which has a 50
100 cm/pixel resolution [*Robinson et al.* 2010]. For typical lunar regolith dielectric properties
101 [*Carrier et al.* 1991], the 12.6 cm wavelength Mini-RF radar wave can penetrate up to ~1 m
102 below the surface. This allows detection of buried impact melt and associated flow structures
103 that have been smoothed over by regolith deposition and maturation and are consequently no
104 longer visible in optical images (e.g. *Campbell et al.* [2010]).
105 Prior radar observations of lunar impact craters using Arecibo Observatory S-band
106 (12.6 cm wavelength) radar system and the Green Bank Telescope have revealed rough, radar
107 bright flows that can extend greater than two crater radii from the rim [*Campbell et al.* 2010].
108 Some of these flows had not been previously identified in imaging data (e.g. Aristillus)
109 [*Campbell et al.* 2010]. The melt flows have very high values of the radar circular polarization
110 ratio, which suggests that the flow surfaces have roughness characteristics greater than

111 terrestrial a'a lavas [*Campbell et al.* 2010]. The Mini-RF radar on LRO can likewise be used
112 to assess melt flow roughness, to determine whether there is structure internal to the flow, and
113 to map flow boundaries, all of which can lead to a better understanding of how impact melt
114 and debris flows are emplaced. Mini-RF has a somewhat higher resolution (15x30 m/pixel)
115 than the highest resolution ground-based radar data (20-30 m/pixel) [*Raney et al.* 2011;
116 *Campbell et al.* 2010]. Mini-RF can also image the lunar farside and the lunar poles to search
117 for examples of impact melts not previously observed by radar.
118
119 **2. Mini-RF Polarimetric Data**
120
121 The Mini-RF instrument on the LRO has acquired S-band (12.6 cm wavelength) radar
122 imagery of many impact craters at a resolution of 15x30 m [*Raney et al.* 2011]. The radar
123 transmits a circular-polarized wave and measures two orthogonal received polarizations
124 (horizontal, H and vertical, V). These data can be used to generate images for each element of
125 the Stokes vector (*Jackson* [1999]; *Green* [1968]):

126 $$S = \begin{bmatrix} S_1 \\ S_2 \\ S_3 \\ S_4 \end{bmatrix} = \begin{bmatrix} \left\langle |E_H|^2 \right\rangle + \left\langle |E_V|^2 \right\rangle \\ \left\langle |E_H|^2 \right\rangle - \left\langle |E_V|^2 \right\rangle \\ 2\mathrm{Re}\left\langle E_H E_V^* \right\rangle \\ -2\mathrm{Im}\left\langle E_H E_V^* \right\rangle \end{bmatrix} \qquad (1)$$

127
128 The first Stokes parameter image (S_1) is a measure of the total average power of the
129 echo. The S_2 and S_3 Stokes parameter images measure the linearly polarized power, and the
130 S_4 Stokes parameter image provides information on the magnitude of the circularly polarized
131 power and whether it is right or left circular-polarized. These four polarization images are a

primary data product of Mini-RF, and are mapped to the lunar coordinate grid with a resolution of 15 m/pixel. The center-swath incidence angle for flat surfaces varies from ~48-55°. Changes in surface topography lead to a large range of incidence angles in many images, particularly images in highland terrains.

The circular polarization ratio (CPR) can be used as an indicator of surface roughness. The CPR, which is the ratio of the same-sense circular polarization as was transmitted to the opposite-sense circular polarization as was transmitted, can be calculated from [*Stacy*, 1993]:

$$CPR = \frac{S_1 - S_4}{S_1 + S_4} \qquad (2)$$

Surfaces that are very smooth at wavelength scales will lead to low CPR values (<0.4), while scattering from surfaces that are rough at the wavelength scale, and have double-bounce geometries, lead to moderate to high (0.4-1.0) CPR values. A double-bounce geometry occurs when the radar wave reflects from two surfaces before returning to the receiver, thereby causing the received circular polarization state to be the same as that transmitted. Extremely rugged terrain can sometimes produce circular polarization ratios greater than one (e.g. *Campbell and Campbell* [1992]; *Campbell* [2009]). These high CPR values cannot be caused by Bragg scattering from wavelength scale roughness (e.g *Ulaby et al.* [1996]) and require that a significant amount of the backscatter come from double-bounce geometries. For terrestrial analog surfaces, CPR values near or above one correspond to surfaces that have a rugged appearance and are rough at centimeter to meter, and sometimes decimeter, scales (e.g. Campbell and Campbell [1992]).

The circular polarization ratio also changes with incidence angle (lunar examples can

be found in *Campbell et al.* [2010], *Carter et al.* [2010], *Carter et al.* [2009]), because at low (nadir) incidence angles, the backscatter is dominated by mirror-like quasi-specular scattering. Therefore, we compare CPR values for surfaces that were observed at similar incidence angles. For this paper, the CPR images were derived by averaging the S1 and S4 images to a resolution of 60 m/pixel and then forming the CPR. This extra averaging reduces the radar speckle noise and therefore improves the visibility of some polarization features.

The Mini-RF data sometimes have a gradient in the circular polarization ratio across the range (or horizontal) dimension of the image and the circular polarization values given in this paper have uncertainties related to this issue. Gradients as large as 0.3 have been measured for a few images, but gradients between 0.1 and 0.2 are more common. These values exceed the change in CPR that could be caused by the few degree incidence angle change across the swath width (range dimension). Prior measurements of the lunar surface at the Mini-RF wavelength (S-band) show that CPR changes by only a few tenths as the incidence angle changes by ~5° [*Campbell et al.* 2010; *Carter et al.* 2009]. For two craters discussed in this paper (Glushko, Aristillus), Mini-RF data was acquired at a similar incidence angle to published ground-based radar data and can be directly compared. In these cases, the CPR values are within 0.05 of those reported in *Campbell et al.* [2010], which suggests that the CPR values measured by Mini-RF are consistent with prior data.

However, for lunar farside craters, there is no alternative data source to check the calibration. In an attempt to mitigate these issues, we have not used CPR measurements in cases where the gradient is particularly bad (e.g. more than +0.1 across the image). Most of the images used in this paper have a CPR gradient less than ~0.05. Because of the general match to ground-based data for the nearside cases, for the low- to moderate-gradient cases

178 used here, we estimate that the systematic errors are no more than ±0.1. Below, we focus on
179 comparing CPR values that are very high (greater than 1), high (0.7-1.0) and moderate (0.6-
180 0.7), to avoid the need for precise CPR numbers. Additional calibration is currently ongoing
181 to improve the quantitative polarimetry from Mini-RF.
182
183 **3. Surface Properties of Melt Flows**
184 Mini-RF has mapped ~66% of the lunar surface at mean incidence angles (on flat
185 terrain) between ~48°-54°, and has imaged many impact craters with ejecta flows and melt
186 ponds. Below, we discuss the surface properties of some of these flow features for craters
187 with different size ranges. The size divisions were chosen to roughly correspond to those used
188 by *Hawke and Head* [1977], who found that the importance of melt flows relative to ponds
189 and veneers varied partially based on impact crater size. The craters discussed here were
190 chosen on the basis of a survey of initial Mini-RF data and are not a statistical sample. In
191 particular, larger melt flows are easier to detect and it is possible that a systematic search of
192 the data will reveal additional small and medium sized craters with impact melt ponds and
193 ejecta flows.
194
195 *3.1 Large (50+ km diameter) impact craters*
196 Impact flows associated with large (>50 km diameter) impact craters display a wide
197 range of morphologies, including ponds and large flows. Melt flows of some craters within
198 this size range can display significant variation in radar backscatter along the flow, and can
199 look similar to radar images of impact crater flows on Venus [*Phillips et al.* 1991; *Chadwick*
200 *and Schaber* 1993]. The 85 km diameter crater Tycho (43.3° S, 248.8° E) is one example

[*Shoemaker et al.* 1968]. Although Tycho is visible in Earth-based radar images, the thin flows are hard to detect in lower resolution Earth-based radar images.

Mini-RF data of flows east of Tycho reveal both dark and bright sections of the melt flow that correspond to smooth and rough surfaces as seen in optical imagery (Figures 1 and 2). The bright areas of the flows typically have high CPR values (1.0-1.2). Radar dark parts of the flow can be difficult to distinguish from the surroundings, particularly since the mountainous terrain leads to a varying radar viewing geometry. However, even the radar-dark portions of the flow have fairly high CPR values, often in the range of 0.8 to 0.9. The lowest CPR values measured for very small parts of the smoothest melt ponds, away from any fresh impact craters or the rough edges of the ponds, are between 0.6 and 0.7. These values are still higher than what is measured for the non-melt flat surfaces in the area (CPR~0.55), and is higher than CPR values measured for most terrestrial a'a flows [*Campbell and Campbell* 1992].

High-resolution LROC NAC images of the upper stages of the flows (Figures 2a and 2b) show the differences in surface texture between smooth ponded melt material and rough flows. The high-CPR areas correspond to a rugged surface that looks similar to upturned platey pahoehoe or a'a flows (Figure 2a). The highest CPR values in this area of the flow are above 1.0, but are obscured by shadow in the LROC image. The CPR values in the non-shadowed rough regions of the LROC image are between 0.9 and 1.0, which is perhaps not surprising given the rugged surface. Nearby smooth areas have small craters, cooling fractures, and large angular blocks. These regions have CPR values of 0.7-0.8, which are still higher than the values measured for most terrestrial lava flows [*Campbell and Campbell* 1992], despite a fairly smooth appearance.

There are a couple of possible explanations for the high CPR values in areas that appear smooth in optical images; either the radar pixels nearly always incorporate enough rough features such as craters, fractures, or blocky regolith to create a high CPR, or the flow surface is very rough at the centimeter scale, possibly due to entrained clasts or to a rugged textured surface that is partially obscured by a coating of regolith. Fractured ponded lava and pahoehoe flows on Earth have CPR values that are lower than a'a lava [*Campbell and Campbell* 1992], so an additional roughness component beyond cooling cracks is likely present. The fact that even very small smooth areas of the melt flow have CPRs that are slightly above the average CPR value in the Tycho extended ejecta blanket suggests that there is a component of centimeter scale surface or near-surface roughness not apparent in current imagery.

The Surveyor 7 spacecraft landed near the rim of Tycho and obtained surface photographs that reveal a complex near-rim geology. The area near the landing site has multiple types of flow-like features that have been attributed to movement of hot gas, debris and melt [*Shoemaker et al.* 1968]. These flows do not have lava-like surface flow features like those seen in the eastern impact melt flows (Figure 2), but the surfaces of the Surveyor 7 flows are still very rough and exhibit varying degrees of cratering, likely from self-secondary impacts [*Shoemaker et al.* 1968]. There are also many fields of angular blocks that are probably fall-back ejecta that was deposited during the later stages of the impact process [*Shoemaker et al.* 1968]. In addition to the rough lava-like flow features apparent in LROC images (Figure 2), secondary cratering of the impact melt and breccia fall-back deposits almost certainly contribute to the high CPR values seen in Figure 1.

246 The radar-bright parts of the Tycho melt flow have a very disrupted surface structure,
247 but in some cases, larger structural trends are present. The flow drains to the southeast,
248 funneling through terrain gaps. It narrows into a thin, channelized flow (with an overprinted
249 crater) before forming a distinct, oblong pond. Within the pond, the Kaguya Terrain Camera
250 images (Figure 2c) show a series of arcuate ridges perpendicular to the flow direction, and a
251 curving boundary that separates the rougher parts of the flow from smoother ponded material.
252 This ridged area is radar bright with high CPR values. These ridges are similar to pressure
253 ridges seen in terrestrial lava flows, which occur when hot, low-viscosity material moves
254 under a partially cooled, higher viscosity surface [*Fink and Fletcher* 1978; *Theilig and*
255 *Greeley* 1986]. In this case, the flow boundary in the middle of the pond (marked with arrows
256 in Figure 2c) may represent the boundaries of a late-stage melt movement into the pond.
257 Alternately, the smooth parts of the pond may have been created by a breakout of melt from
258 an initial rough flow that subsequently filled in the area to the south.
259 The surface texture of the pond suggests a complex formation process that may have
260 included multiple influxes of melt that pushed into the pond, and created rough terrain or
261 breakouts, after the flow had partially cooled. Different flow structures are present to the
262 north, where the Mini-RF data show sinuous radar-bright, high-CPR paths that track rougher
263 terrain along the flow direction or at flow terminal areas. These include one area where rafted
264 plates of melt were transported downstream (Figure 2b).
265 The longest flows observed to date are associated with the 55 km diameter crater
266 Aristillus (33.9° N, 1.2° E) [*Campbell et al.* 2010]. These flows are long, thin, and extend
267 over 2 crater radii from the rim [*Campbell et al.* 2010]. In contrast to Tycho, there is little
268 change in backscatter cross-section along the flow and no evidence of channeling. In addition

to these long flows, small ponds occur close to the crater rim, and are visible in both optical and radar data. In Mini-RF data, the margins of the long flows have a complex shape that was generated as the melt flowed around multiple topographic obstacles (Figure 3). Most of the radar bright areas are connected, suggesting that the melt was mostly deposited as a topography-constrained flow rather than as individual ponds, although some of the radar bright areas do not have any apparent connection to the main flow. Similar thin melt flows on Venus appear to be caused when melt flows along thin valleys or fractures [*Asimov and Wood* 1992; *Chadwick and Schaber* 1993]. The high radar backscatter of the melt deposits suggests that their surface is very rough. The CPR values of the melts are around 0.65 (Figure 3c), which is higher than those of the surrounding terrain, but lower than those of the Tycho melt flows, probably because Aristillus at ~2.1 Ga [*Ryder et al.,* 1991] is significantly older than Tycho (~100 Ma; *Arvidson et al.* [1976]).

The melt flow is barely visible in optical images and looks very similar to surrounding mare basalts. Images acquired with the Kaguya Terrain Camera (10 m/pixel resolution) (Figure 3d) do not show flow features within the radar bright areas, suggesting that the flows are covered by a thin regolith layer. Given the penetration depth of the radar, the surface covering is likely less than a meter. This mantling layer could also explain the lower CPR values, since the radar backscatter would include contributions from both the surface regolith and subsurface rough melt deposit. Because the flow is buried under a greater amount of material than the Tycho melt flow, it is possible that there are smooth parts of the melt flow that are not visible in the radar data; such areas may link some of the distal deposits that appear unconnected in the radar data. Alternatively, some of the unconnected sections of the flow could be ponds that formed when ballistically ejected melt was trapped in depressions.

The fresh crater Jackson (71 km diameter) on the far side of the Moon is similar in size to Tycho and also has a large ray system. Radar images to the east of the crater show features with a flow-like morphology that are significantly different from the impact melt flows described above. Figure 4a is a LROC Wide Angle Camera (WAC) mosaic image of the area, and Figure 4b shows the Mini-RF total power images on a WAC background with the flow features marked with arrows. The circular polarization ratio images are shown in Figures 4c and 4d. In this case, it looks like material has flowed around and over a series of crater walls (arrows in Figure 4).

The flows have moderate backscatter in the central areas, but are sometimes brighter at the margins and in places where the flows have a contact with an abrupt topographic change (Figure 4b). The lack of radar-bright backscatter from the central regions suggests that the flows are not as rugged as some parts of the melt flows observed at Tycho and Aristillus. The circular polarization ratio values of the flows are higher than surrounding terrain in some areas, but in other places the flows have CPR values that are very similar to the Jackson distal ejecta (Figures 4c and d). The flows do not show a distinct high-CPR contrast with their surroundings like the melt flows at Tycho and Aristillus, which suggests that the Jackson flow features may be composed primarily of blocky ejecta. The radar bright flow edges may be caused by rough deposits or by higher topography at the edges of the flow. Since there is no evidence for flowing melted or ponded rock in either radar or optical images, the Jackson flow features may have been caused by debris flows that entrained dust, rock, and small amounts of melt and deposited material at topographic boundaries. These flows may be more similar to some of the debris-rich flows observed in Surveyor 7 images of Tycho than they are to the Tycho melt flows [*Shoemaker et al.* 1968].

315

316 *3.2 Medium-sized craters (20-50 km diameter)*

317 Prior imaging analyses have shown that craters in this size range often have significant
318 amounts of melt material that can flow large distances from the source crater [*Hawke and*
319 *Head* 1977]. The 43 km diameter crater Glushko (a.k.a. Olbers A; 8° N, 282.4° E) is a good
320 example. Glushko has a complex melt flow pattern similar to that observed at Tycho (Figure
321 5). LROC Narrow Angle Camera (NAC) images show pressure ridges similar to those seen at
322 Tycho (Figure 5c), but there do not appear to be areas of overturned and rafted plates. Radar-
323 dark areas within the melt flow correspond to cratered ponded areas with fractures. In optical
324 images, the surface of the flow is smoother and the flow features are less pronounced than
325 they are for the Tycho flow, suggesting that the surface may be covered by a thicker layer of
326 regolith.

327 The 26 km diameter crater Gerasimovich D (22.3° S, 238.4° E) also has significant
328 melt deposits, despite not having a radar bright proximal ejecta blanket. A radar-bright impact
329 melt flow extends ~2 crater radii from the rim (Figure 6). The melt flow is barely visible in
330 LROC WAC optical images but has a subdued appearance probably caused by regolith cover
331 (Figure 6a). The flow has a fairly uniform radar brightness compared to the Tycho and
332 Glushko melt flows (Figure 6b), but minor variations are still present. These may be caused
333 by slight differences in the surface texture of the buried flow, or possibly due to smoothing by
334 varying amounts of surface coating. The CPR values are high (0.75), as they are for other
335 radar-bright melt flows.

336 Another example is the well-known crater Wiener F (47 km diameter; 41.2° N, 150°
337 E), which has both a melt flow and a ponded deposit (Figure 7). Radar images show that the

338 pomd is bright with an average CPR value of 0.98. The melt pond surface is rough and
339 ridged, similar to parts of Tycho and Glushko (Figure 7a). A bright flow feature is visible on
340 the pre-existing crater wall that faces towards the impact site. Lunar Orbiter images have a
341 favorable lighting geometry that show a ridge of material corresponding to the radar features.
342 The radar-bright flow on the wall may be either a melt flow that traveled up the wall, a blocky
343 debris flow that was pushed up the wall, or a melt veneer in which the mobile melt drained
344 back into the crater, leaving a lag deposit of unmelted clasts. The rough surface and flow
345 features present on the melt pond surface suggest that the melt was not tightly constrained
346 within the topographic boundaries of the preexisting crater, so it was able to flow and develop
347 complex surface features that were frozen in place as it cooled.
348
349 *3.3 Small craters (<20 km diameter)*
350 *Hawke and Head* [1977] observed that large amounts of impact melt first begin to be
351 seen surrounding craters between 10 and 20 km diameter. Mini-RF images of craters within
352 this size range reveal mostly radar bright ponds, veneers, and small flows.
353 A small, 13.5 km diameter unnamed rayed crater at 30.9° S, 145.5° E (south of Pavlov
354 G) has melt deposits close to its rim. Mini-RF images show a small, radar-bright flow and
355 pond extending ~1 crater radii away from the rim (Figure 8). Like many of the ponds
356 associated with larger craters, the circular polarization values are high and well matched to
357 those of the surrounding ejecta blanket. There are no radar backscatter changes within the
358 melt, suggesting a small amount of melt that cooled quickly.
359 Another unnamed 13 km diameter crater at (35.7° N, 166.0° E, west of Hutton)
360 appears to have a radar flow or bright ejecta extending from the western edge of the crater rim

(Figure 9). The bright melt has an unusual dark lane extending from the rim to the base of the melt. The dark lane has rounded edges and a small offshoot that could indicate that it was caused by some type of flow. Kaguya Terrain Camera imagery (Figure 9c) does not show any obvious explanation for the difference in radar backscatter. The circular polarization ratio image (Figure 9b) shows that the radar-bright ejecta has a high circular polarization ratio, which is consistent with a rough surface of proximal ejecta or melt. The radar-dark lane, however, has a very low CPR, which suggests scattering from terrain that has fewer rocks and more fine material than the surrounding regions. The dark lane may be the result of a landslide or small debris flow from the steep crater rim that left a coating of fine-grained material or removed large blocks. Alternatively, the radar-dark feature may be fine-grained material deposited as part of the impact process.

In another case, possible ejecta flow features are associated with a small, fresh 5 km diameter crater to the northeast of Maunder, in the Orientale basin (Figure 10). In this case, a radar bright deposit appears to have moved downhill to the south and around the topographic contours of Maunder. The radar-bright feature extends ~12 crater radii from the rim. This is a relatively long distance for such a small crater, although there is also a significant downhill slope into Orientale basin in this area. The radar-bright areas do not have flow features (e.g. pressure ridges or channels) associated with them (Figure 10c), and they are optically bright and appear to lie in topographic depressions. Because the distal crater ejecta extends almost as far as the radar-bright feature (10 crater radii in this area), all of the radar-bright areas along the edge of Maunder crater may be rough ejecta from the impact, rather than a melt flow.

To the northwest, there are surface ripples extending out to 6 crater radii, and the bright distal ejecta continue even farther, out to about 9 crater radii. The radar image shows

384 flow features on the side of a low hill that faces away from the impact site (Fig. 10a). This
385 feature is darker than most of the crater ejecta in the radar images, and optical images from
386 the Kaguya Terrain Camera show that it is bright, slightly raised terrain (Figure 10b). The
387 CPR values across the flow features are similar to those of the surrounding hills. This may be
388 part of a debris flow from the impact that flowed across the low hills, similar to what is seen
389 at Jackson.
390
391 *3.4 Melt deposits with ambiguous sources*
392 Two areas appear to have flows and ponds of impact melt that do not have a clear
393 source. One such example is the western side of Keeler crater (11° S, 157° E), where the radar
394 images reveal bright ponds and flows (Figure 11, 12). Some, but not all, of the melt features
395 are visible in Kaguya Terrain Camera images (Figure 11b, 12). The radar bright ponds have
396 CPR values (~0.7) much higher than the surrounding terrain (~0.3) and similar to those
397 measured for other melt deposits, suggesting that the features are impact melt related and not
398 smooth, block-poor deposits of fine-grained dust. Another similar area at around 41° N and
399 166° E was identified by *Robinson et al.* [2011] and has similar radar properties, including
400 radar bright ponds and flow features (Figure 13). The ponds are more distinct at this site, and
401 have significantly higher CPR values, possibly because they are less regolith-covered than the
402 Keeler flows and ponds. The high-resolution NAC frames of these features show abundant
403 surface texturing and block fields, consistent with high radar backscatter [Robinson et al.,
404 2011].
405 Unlike the other flows and ponds discussed in prior sections, these features are not
406 clearly associated with the rim or ejecta blanket of a specific crater. Instead, melt appears to

have flowed downhill into many topographic lows covering a broad area. One possible explanation is that the melts were produced by oblique impacts that deposit a significant amount of melted material downrange, or to the sides of, the impact site. Similar features exist on Venus; for example, at Graham crater (1° N, 6° E), where some material is trapped in small ponds on a hill [*Schultz* 1992]. However, oblique impacts on the smooth Venus plains also generate significant flow features, in part because of the higher temperatures and higher mean impact velocities that produce a larger amount of melt, and in part because the terrain is often not rugged enough to trap the melt in many small ponds.

Identifying a source crater for the extensive melt deposits is difficult in the heavily cratered highlands. For example, the Keeler site has a young impact crater (Ventris M) to the north with a ray system that is noticeably symmetric, although the crater rim is slightly elliptical. However, the crater is ~120 km distant, and there is no evidence for extensive melt deposits near the crater itself. Another nearby oblique impact crater is Keeler V, but in this case, some of the impact melt clearly flows over the rim and into the Keeler V floor (Figure 11d), which suggests a different source. Keeler V is also older and more degraded than other nearby craters, so it is unlikely to have retained clear melt deposits. The source crater may also have been a nearby, less oblique impact that did not produce a crater rim that deviates from circular. The 37 km diameter crater Plante′, inside Keeler crater, has impact melt flows extending from the proximal ejecta blanket, but is also over 100 km distant. The crater Keeler S is the closest crater to the site. It does not have a radar bright ejecta blanket or evidence of near-rim melt deposits, but neither does Gerasimovich D, which has a large melt flow. Regardless of the source, these isolated melt deposits are interesting in that they suggest that impact melts may cover substantial areas even in heavily cratered terrains and may remain

430 visible even as the source crater proximal ejecta ages and weathers to blend into the
431 surrounding terrain.
432
433 **4. Discussion**
434
435 The radar data described above can be used to assess the surface roughness of the
436 lunar impact melts compared to terrestrial lava flows. Many of the melt flows have a very
437 uniform, radar bright appearance, as reported by *Campbell et al.* [2010]. However, in some
438 cases, the flow changes both in backscatter and circular polarization ratio along the flow.
439 Terrestrial a'a flows have CPRs between 0.3 and 0.6 at incidence angles of 40-50 [*Campbell*
440 *and Campbell* 1992]. Blocky lava flows like SP Flow (north of Flagstaff, Arizona) have CPRs
441 of 0.8-1.2 at the same incidence angles, at 24 cm wavelength [*Campbell and Campbell* 1992].
442 At shorter wavelengths, the flows have somewhat higher CPR values. The CPR values of the
443 radar bright lunar melt flows are often greater than those of terrestrial a'a flows and similar to
444 those of blocky lava flows like SP Flow, which suggests that the flows have extremely rugged
445 surfaces at centimeter to meter scales. In cases where the CPR values of the bright flows are
446 somewhat lower in some of the older craters (e.g. Aristillus, Gerasimovich D) the melt flows
447 appear partially buried in optical images, which likely reduces the CPR. Ponded deposits that
448 appear smooth in optical data still have CPR values as great as terrestrial a'a flows [*Campbell*
449 *and Campbell* 1992], probably due to a combination of initial rough surface texture
450 subsequently filled in by dust, fallback breccia deposited on the surface, the presence of small
451 impact craters and related blocky ejecta, surface cooling fractures, and embedded county rock
452 clasts.

453 So far, within the resolution limit of the Mini-RF radar, there are no examples of small
454 craters (<20 km) with complex flows showing significant backscatter and circular polarization
455 ratio variations along the flow. The impact melt deposits of small craters are always radar-
456 bright with high CPR values. The surfaces of many of the small flows and ponds may have
457 cooled fairly quickly, before they had time to form smooth surfaces. In the case of larger
458 craters, like Tycho and Glushko, late stage injection of melt from draining ponds at higher
459 elevations may have broken up a previously frozen surface and created a very rugged and
460 broken terrain.
461 In some cases, particularly for rough radar-bright flows, the radar data often provides a
462 more useful view of flow margins than optical data, where the surface can be mantled by fine-
463 grained regolith. Young impact craters, such as Tycho, have relatively unburied melts that are
464 readily apparent in both radar and optical data. Many of the melt deposits and flows described
465 here are associated with craters that have ray systems and hence are geologically young. Over
466 time, the crater ejecta, including ray systems and ejecta flows, are destroyed and buried by
467 subsequent impacts.
468 *Ghent et al.* [2005] showed that younger craters often have radar-dark haloes in 70-cm
469 wavelength radar data, and that older craters do not have these haloes. These haloes have been
470 attributed to a layer of fine-grained ejecta mantling that becomes mixed into the underlying,
471 blocky ejecta blanket over time [*Ghent et al.* 2005]. Two of the features with impact melts
472 have radar dark haloes (Tycho and Aristillus), but the others discussed above are located on
473 the lunar limb or farside where no 70-cm wavelength radar data is currently available. There
474 is clearly a process by which ray systems, radar dark haloes, and ejecta flow features are
475 erased, but it is not yet clear what timeline this process follows or how it varies with crater

476 size. Future comprehensive searches of the radar data will help to improve the statistics of
477 which types and ages of craters have melt deposits and ejecta flows.
478 The combination of radar and optical data for the lunar impact melts also has some
479 implications for the surface textures of impact melt flows on Venus, for which only radar data
480 is available. In particular, as proposed by *Johnson and Baker* [1994], the lunar data suggest
481 that many of the changes in radar reflectivity within large complex melt flows are probably
482 due to flow features similar to those seen in terrestrial lava flows, such as ponding, rafted and
483 overturned plates, channeling, and pressure ridges. Some of the Venus flows appear darker to
484 the radar and have been interpreted as turbulent run-out flows that carry debris [*Schultz* 1992].
485 These Venus flows have some similar radar characteristics to the flows associated with
486 Jackson and the small crater near Maunder, which are darker to the radar and show no optical
487 evidence for flowing, melted rock. The impact process may sometimes produce debris flows
488 that are visible in radar images due to the sharp contrast in topography and roughness of the
489 emplaced material relative to the surroundings.
490
491 **4. Summary and Future Work**
492 Recent radar imaging data suggests that impact melt flows and ponds are more
493 common on the Moon than was previously known. The CPR values of the melt flows are
494 generally high and most of the flows have very rugged surfaces. Some lunar impacts cause
495 debris to be deposited in a flow-like manner, and these flows are often visible in radar images
496 due to their rough edges and topographic expression. Future work will aim to achieve better
497 statistics on the number and size of craters with melt flows and ponds. The Mini-RF data will
498 be useful for understanding the amount of melt produced by impacts, as well as the directions

499 in which most of the melt traveled. A systematic search of young and rayed crater systems
500 using high resolution radar imaging is likely to yield additional data on buried and partially
501 buried melt flows, including how the melt flows are buried and eroded over time.
502
503 **Acknowledgements:** We thank the Mini-RF engineering and operations teams for their work
504 in building the instrument and acquiring the data. We also thank the LRO LROC and Kaguya
505 (SELENE) Terrain Camera teams for their efforts to provide the publicly available data sets
506 used in this work. Thanks to Veronica Bray and Wenzhe Fa who provided detailed and
507 helpful reviews. This project was supported through a NASA LRO Participating Scientist
508 grant (NNX08AM80G) to L. Carter.
509
510

510 **References**

511

512 Arvidson R., R. Drozd, E. Guiness, C. Hohenberg, C. Morgan, R. Morrison and V. Oberbeck
513 V (1976), Cosmic ray exposure age of Apollo 17 samples and the age of Tycho. *Proc. Lunar*
514 *Sci. Conf. 7*, 2817-2832.

515

516 Asimow, P. D. and J. A. Wood (1992), Fluid Outflows from Venus Impact Craters: Analysis
517 from Magellan Data, *J. Geophys Res., 97*, E8, 13643-13665.

518

519 Bray, V. J., L. L. Tornabene, L. P. Keszthelyi, A. S. McEwen, B. R. Hawke, T. A. Giguere, S.
520 A. Kattenhorn, W. B. Garry, B. Rizk, C. M. Caudill, L. R. Gaddis, and C. H. van der Bogert
521 (2010), New Insight into Lunar Impact Melt Mobility from the LRO Camera, *Geophys. Res.*
522 *Lett., 37*, L21202, doi:10.1029/2010GL044666.

523

524 Campbell, B. A. and D. B. Campbell (1992), Analysis of volcanic surface morphology on
525 Venus from comparison of Arecibo, Magellan, and terrestrial airborne radar data, *J. Geophys.*
526 *Res., 97 (E10)*, 16293-16314.

527

528 Campbell, B. A. (2009), Scale dependent surface roughness behavior and its impact on
529 empirical models for radar backscatter, *IEEE Trans. Geosci. Rem. Sens. 47*,
530 doi:10.1109/TGRS.2009.2022752, 3480-3488.

531

532 Campbell, B. A., L. M. Carter, D. B. Campbell, M. C. Nolan, J. F. Chandler, R. R. Ghent, B.
533 R. Hawke, R. F. Anderson and K. S. Wells (2010), Earth-Based S-band Radar Mapping of the
534 Moon: New Views of Impact Melt Distribution and Mare Physical Properties, *Icarus*, *208*,
535 doi:10.1016/j.icarus.2010.03.011.
536
537 Carrier, W. D., G. R. Ohloeft and W. Mendell (1991), Physical properties of the lunar surface,
538 in *Lunar Sourcebook*, 475-567, Cambridge Univ. Press, New York.
539
540 Carter, L. M., D. B. Campbell and B. A. Campbell (2011), Geologic studies of planetary
541 surfaces using radar polarimetric imaging, *Proc. IEEE, 99*,
542 doi:10.1109/JPROC.2010.2099090.
543
544 Chadwick, D. J. and G. G. Schaber (1993), Impact Crater Outflows on Venus: Morphology
545 and Emplacement Mechanisms, *J. Geophys. Res., 98*, 20891-20902.
546
547 Fink, J. H. and R. C. Fletcher (1978), Ropy Pahoehoe: Surface Folding of a Viscous Fluid, *J.*
548 *Volcan. Geothem. Res., 4*, 151-170.
549
550 Ghent, R. R., D. W. Leverington, B. A. Campbell, B. R. Hawke and D. B. Campbell (2005),
551 Earth-based observations of radar-dark crater haloes on the Moon: Implications for regolith
552 properties, *JGR*, *110*, E02005, doi:10.1029/ 2004JE002366.
553
554 Green, P. E (1968), Radar Measurements of Target Scattering Properties, in Radar

555 Astronomy, eds. J. V. Evans and T. Hagfors, McGraw-Hill, New York, New York.
556
557 Guest, J. E. (1973) Stratigraphy of ejecta from the lunar crater Aristarchus, *Geol. Soc.*
558 *America Bull., 84*, 2873-2894.
559
560 Hawke, B. R. and J. W. Head (1977), Impact melt on lunar crater rims, in Impact and
561 Explosion Cratering, eds. D. J. Roddy, R. O. Pepin and R. B. Merrill, Pergamon Press, New
562 York, pp. 815-841.
563
564 Howard, K. A. and H. G. Wilshire (1975), Flows of impact melt at lunar craters, *J. Res. U. S.*
565 *Geol. Survey, 3*, no. 2, 237-251.
566
567 Jackson, J. D. (1999), Classical Electrodynamics, Third Edition, John Wiley and Sons, New
568 York, New York.
569
570 Johnson, J. R. and V. R. Baker (1994), Surface Property Variations in Venusian Fluidized
571 Ejecta Blanket Craters, *Icarus, 110*, 33-70.
572
573 Phillips, R. J., R. E. Arvidson, J. M. Boyce, D. B. Campbell, J. E. Guest, G. G. Schaber and L.
574 A. Soderblom (1991), Impact Craters on Venus: Initial Analysis from Magellan, *Science, 252*,
575 288-296
576
577 Pierazzo, E. and H. J. Melosh (2000), Melt Production in Oblique Impacts, *Icarus, 145*, 252-

261.

Raney, R. K., P. D. Spudis, B. Bussey, J. Crusan, J. R. Jensen, W. Marinelli, P. McKerracher, C. Neish, M. Palsetia, R. Schulze, H. B. Sequeira, and H. Winters (2011), The Lunar Mini-RF Radars: Hybrid Polarimetric Architecture and Initial Results, *Proc IEEE, 99*, doi: 10.1109/JPROC.2010.2084970, 808-823.

Robinson, M. S., and 22 coauthors (2010), Lunar Reconnaissance Orbiter Camera (LROC) instrument overview, *Space Sci. Rev., 150*, 81–124, doi:10.1007/s11214-010- 9634-2.

Robinson, M. S., P.C. Thomas, B. W. Denevi, T. Tran, E. B. Cisneros, J. Plescia, C. H. van der Bogert, and H. Hiesinger (2011), Highland Plains, an Exceptional Grouping, 42nd Lunar Plan. Sci. Conf., abstract #2511.

Ryder G., D. Bogard and D. Garrison (1991), Probable age of Autolycus and calibration of lunar stratigraphy, *Geology, 19*, 143-146.

Schultz, P. H. (1992) Atmospheric Effects on Ejecta Emplacement and Crater Formation on Venus from Magellan, *J. Geophys. Res., 97*, E10, 16183-16248.

Schultz, P. H. (1996), Effect of impact angle on vaporization, *J. Geophys. Res., 101*, E9, 21117-21136.

601 Shoemaker E.M., R. M. Batson, H. E. Hole, E. C. Morris, J. J. Rennilson and E. A. Whitaker
602 (1968), Television observations from Surveyor VII. In Surveyor VII: A Preliminary Report,
603 *NASA SP-173*, 13-81.
604
605 Stacy, N. J. S. (1993), High resolution synthetic aperture radar observations of the Moon, PhD
606 dissertation, Dept. of Astronomy, Cornell University.
607
608 Theilig, E. and R. Greeley (1986), Lava Flows on Mars: Analysis of Small Surface Features
609 and Comparisons with Terrestrial Analogs, *J. Geophys. Res., 91*, B13, E193-E206.
610
611 Ulaby, F. T., R. K. Moore, and A. K. Fung (1986), Microwave Remote Sensing: Active and
612 Passive, Volume 2, Artech House, Norwood, Massachusetts.

613

Figures:

Figure 1: Mini-RF images of impact melt deposits to the east of Tycho. (a) A total power radar backscatter image. Radar illumination is from the left. (b) A CPR image stretched to a color scale and overlaid on the total power image. The Tycho ejecta deposits have very high CPR values, but the values are particularly large in radar-bright areas that correspond to very rugged impact melt flows. The positions of Fig. 2b and 2c are marked on (a).

Figure 2: Surface textures associated with different radar backscatter characteristics. (a) High-resolution images from LROC NAC (M116372249) show highly disrupted terrain that corresponds to CPR values greater than one. The roughest areas have ridges, mounds, and upturned plates. (b) An LROC NAC image (M119916367) showing rafted plates. These areas also have elevated CPR values, although the values remain below one. (c) A Kaguya Terrain Camera image showing a section of the southern melt flow and pond. The position of Fig 2a is marked with a white box. The outline of an area of pressure ridges within the pond is marked with arrows. This may represent late stage flow into the pond; alternatively, the pond may have formed via a breakout from an initially smaller flow. Parts (b) and (c) are marked on the radar image in Figure 1.

Figure 3: Four images of the impact melt flows northeast of Aristillus. (a) A context image from the LROC WAC mosaic. (b) Mini-RF total power image; radar illumination is from the right. The radar-bright impact melts are mostly connected, but some isolated ponds are present. (c) Mini-RF CPR image, stretched to a color scale and overlaid on the total power

image. The impact melts have higher CPR values than the surrounding terrain, but they are less than what is measured for Tycho. The gradient across the image is due to the calibration errors discussed in section 2. (d) Kaguya Terrain Camera image of the same area. The melt flows are barely visible and have been smoothed over by a regolith coating.

Figure 4: Flow features east of Jackson crater. (a) An LROC WAC context image showing the location of the radar data. (b) Radar total power images (left and right sides) overlaid on the WAC image. Radar illumination is from the right. Arrows mark the positions of flow-like features. Although the features are somewhat brighter than their surroundings, they are not as bright and well-defined as the Tycho and Aristillus melt flows. (c) CPR image of the western (left) radar image in (b), generated by stretching the CPR data to a color scale and overlaying on the total power image. (d) A CPR overlay of the eastern (right) radar image in (b). Parts of the flow features have CPR values that are slightly elevated compared to nearby terrain, but the CPR values are not distinctly different from the proximal ejecta, as is seen at Tycho and Aristillus. Optical images show no evidence of ponded melt. These features may be generated by debris flows.

Figure 5: Flows north of the crater Glushko. (a) Mini-RF total power image. Radar illumination is from the right. The location of the image in part C is shown with a box. (b) CPR image stretched to a color scale and overlaid on the total power image. (c) An LROC NAC image of part of the Gluskho flows. As with Tycho, radar-bright, high CPR parts of the flow have rugged flow features, such as pressure ridges. The flow features are not pronounced as they are for Tycho, and the surface may have a thicker mantling layer.

659

660 **Figure 6:** Impact melt flows west of the crater Gerasimovich D. (a) An LROC Wide-Angle
661 Camera image of the crater and surrounding area. The impact melt flows are visible in some
662 places, but are generally covered by regolith. (b) Mini-RF total backscatter power images.
663 Radar illumination is from the left. The radar wave penetrates through thin regolith cover to
664 reveal the flow outlines. The flow has a fairly uniform radar brightness compared to the
665 Tycho and Glushko flows, but there are subtle brightness changes that may indicate smoother
666 and rougher parts of the buried flow or variations in regolith depth.

667

668 **Figure 7:** The Wiener F flow and pond. (a) High-resolution Lunar Orbiter images (LO5-
669 103H2 and H3) have a lighting geometry that highlights the structure of the melt pond. The
670 pond has rough ridges on the surface. North is to the right in this image. Arrows highlight the
671 same features in both images: the edge of the melt pond and a flow feature higher on the rim.
672 (b) Mini-RF total power image of the pond. North is to the right, and the radar illumination is
673 from the top. The flow feature on the crater wall is particularly apparent in the radar data.

674

675 **Figure 8:** Mini-RF images of a pond associated with a small (13.5 km), unnamed crater
676 (30.9° S, 145.5° E). (a) The total power backscatter radar image. Radar illumination is from
677 the left, and the position of image part C is shown with a box. (b) The circular polarization
678 ratio, stretched to a color scale and overlaid on the total power image. The pond is radar-
679 bright with high CPR values. (c) Total power image of the small pond, which is cratered.

680

Figure 9: An unnamed 13-km diameter crater (35.7° N, 166.0° E) with an unusual radar-dark lane on top of a possible melt flow or veneer. (a) The radar total power image; illumination is from the left. The location of the Kaguya image in part c is marked with a box. (b) The circular polarization ratio image stretched to a color scale and overlaid on the total power image. (c) A Kaguya image of part of the impact melt and radar-dark region. There is no obvious surface expression of the radar-dark lane. Arrows in (a) and (b) mark the location of a thin outshoot of the dark lane that has rounded edges suggestive of some type of flow.

Figure 10: Images of flow features associated with a small (5 km diameter) crater northeast of Maunder crater in the Orientale basin. North is towards the top of the images. (a) A radar total-power image mosaic; illumination is from the left. The location of the images in parts b and c are marked with boxes. Arrows mark the location of flow-like features distant from the central crater. (b) A Kaguya Terrain Camera image of a flow feature northwest of the crater. The feature corresponds to an area of bright debris that appears to have flowed downhill into a valley. (c) A Kaguya Terrain Camera image of radar-bright crater ejecta that has been deposited along the rim of Maunder crater.

Figure 11: Images of ponds and flows near Keeler crater. Most of the melt is north of the crater Keeler S. (a) A LROC WAC context image with craters labeled. A box marks the locations of parts b and d. (b) A Kaguya Terrain Camera image of the area of ponds. Some of the more easily visible ponds are marked with arrows. An arrow also marks the location of a small pond and flow that is easily visible in the radar data. A box marks the area covered by the close-up images in Figure 12. (c) A circular polarization ratio image of part of the melt

704 pond field. This image corresponds to the left-most radar image in part d. The location of the
705 small pond and flow is marked. Most of the ponds have CPR values between 0.6 and 0.7,
706 suggesting that they are rougher than their surroundings, but probably partially buried. (d)
707 Radar total backscatter images of the area shown in part b. The backscatter images show
708 multiple radar-bright ponds and flow features, including flows into Keeler V. Radar
709 illumination is from the left.
710
711 **Figure 12:** A close-up view of Keeler-area melt ponds and flows. The image location is
712 marked in Figure 11. (a) Kaguya image with ponds marked. (b) Corresponding total power
713 radar image. Note that in the optical image, the illumination is from the right but in the radar
714 image, the illumination is from the left. Arrows mark the position of ponded material at the
715 bottom of a hill. The radar image shows a radar bright streak that could be melt material that
716 flowed down the side of the hill. On the right side of the optical image, there is a pond that
717 does not appear to show up in the radar data, probably because the radar viewing geometry
718 shifts the bottom of the crater off the edge of the image. An additional, barely visible, pond is
719 visible in the lower right of the image. Arrows mark the pond and a slightly flat sinuous ridge
720 leading down to the pond.
721
722 **Figure 13:** Mini-RF images of the pond field located at 41° N and 166° E [*Robinson et al.*
723 2011]. (a) Total backscatter power. (b) Circular polarization ratio image stretched to a color
724 scale and overlaid on the total power image. The ponds at this site have higher CPR values
725 than the ponds at Keeler, but they also appear to be less buried in both radar and optical
726 imagery [*Robinson et al.* 2011]. Radar illumination is from the left.

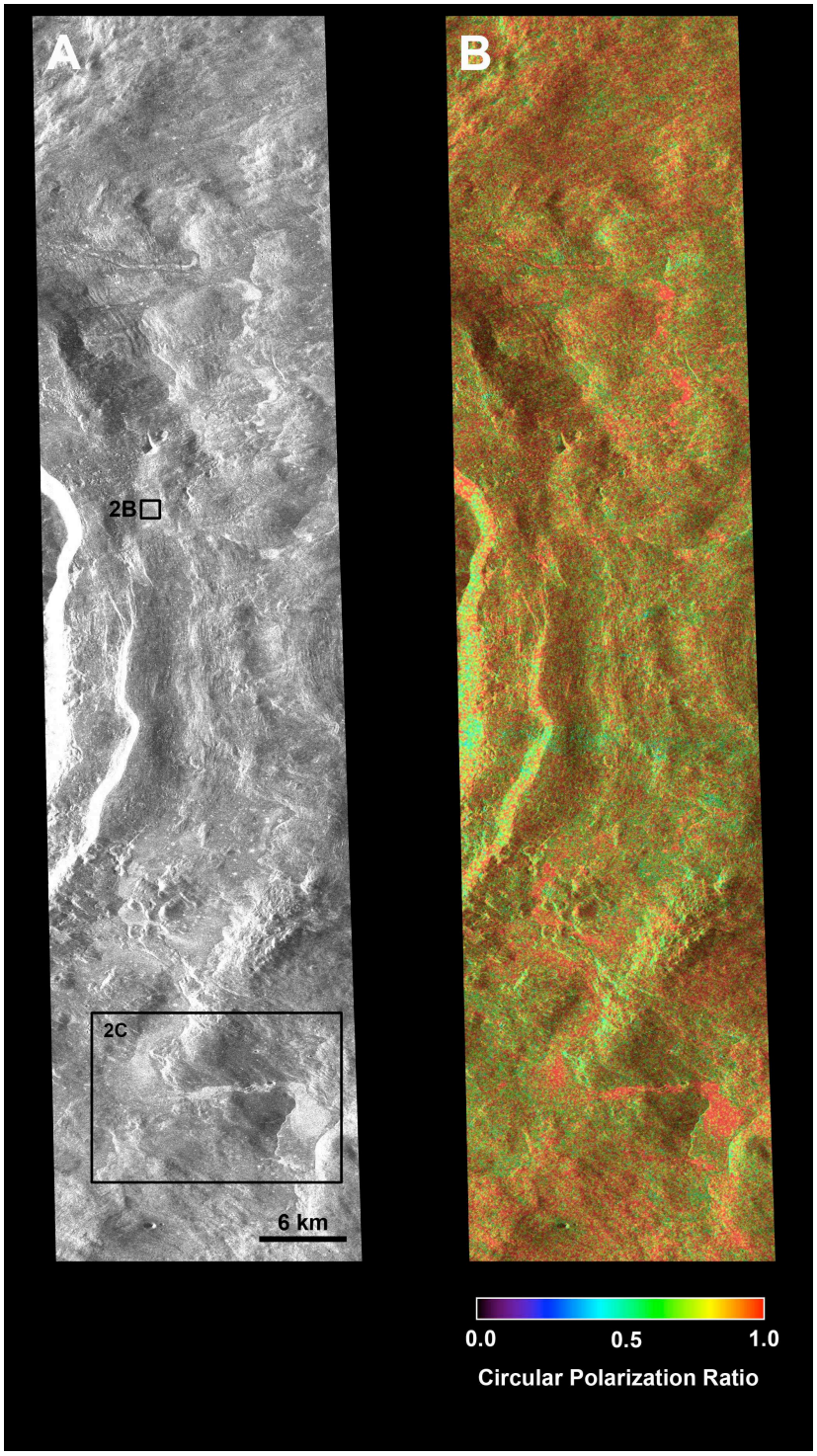

727

728 **Figure 1:** Mini-RF images of impact melt deposits to the east of Tycho. (a) A total power
729 radar backscatter image. Radar illumination is from the left. (b) A CPR image stretched to a
730 color scale and overlaid on the total power image. The Tycho ejecta deposits have very high
731 CPR values, but the values are particularly large in radar-bright areas that correspond to very
732 rugged impact melt flows. The positions of Fig. 2b and 2c are marked on (a).

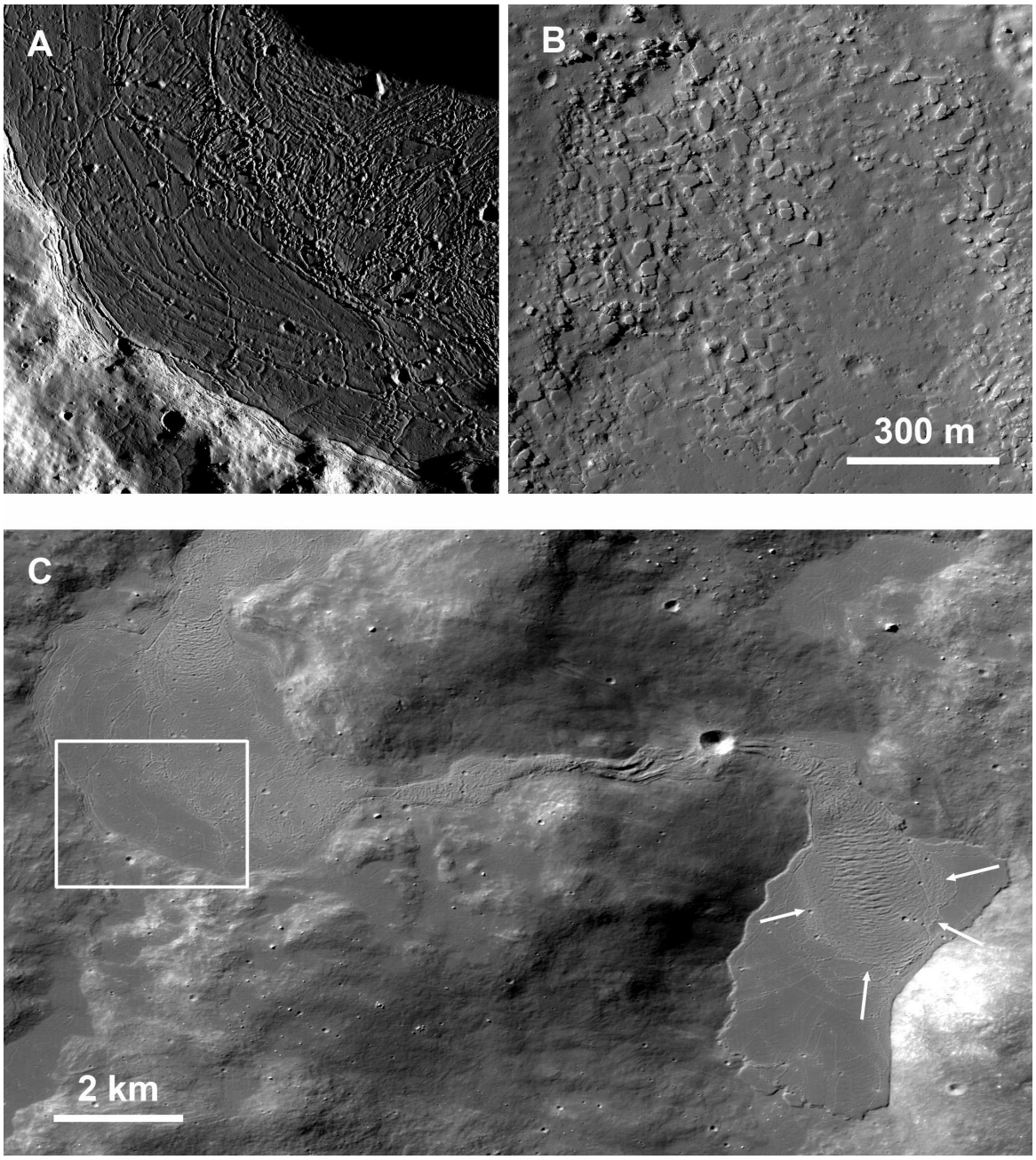

Figure 2: Surface textures associated with different radar backscatter characteristics. (a) High-resolution images from LROC NAC (M116372249) show highly disrupted terrain that corresponds to CPR values greater than one. The roughest areas have ridges, mounds, and upturned plates. (b) An LROC NAC image (M119916367) showing rafted plates. These areas also have elevated CPR values, although the values remain below one. (c) A Kaguya Terrain Camera image showing a section of the southern melt flow and pond. The position of Fig 2a is marked with a white box. The outline of an area of pressure ridges within the pond is marked with arrows. This may represent late stage flow into the pond; alternatively, the pond may have formed via a breakout from an initially smaller flow. Parts (b) and (c) are marked on the radar image in Figure 1.

745

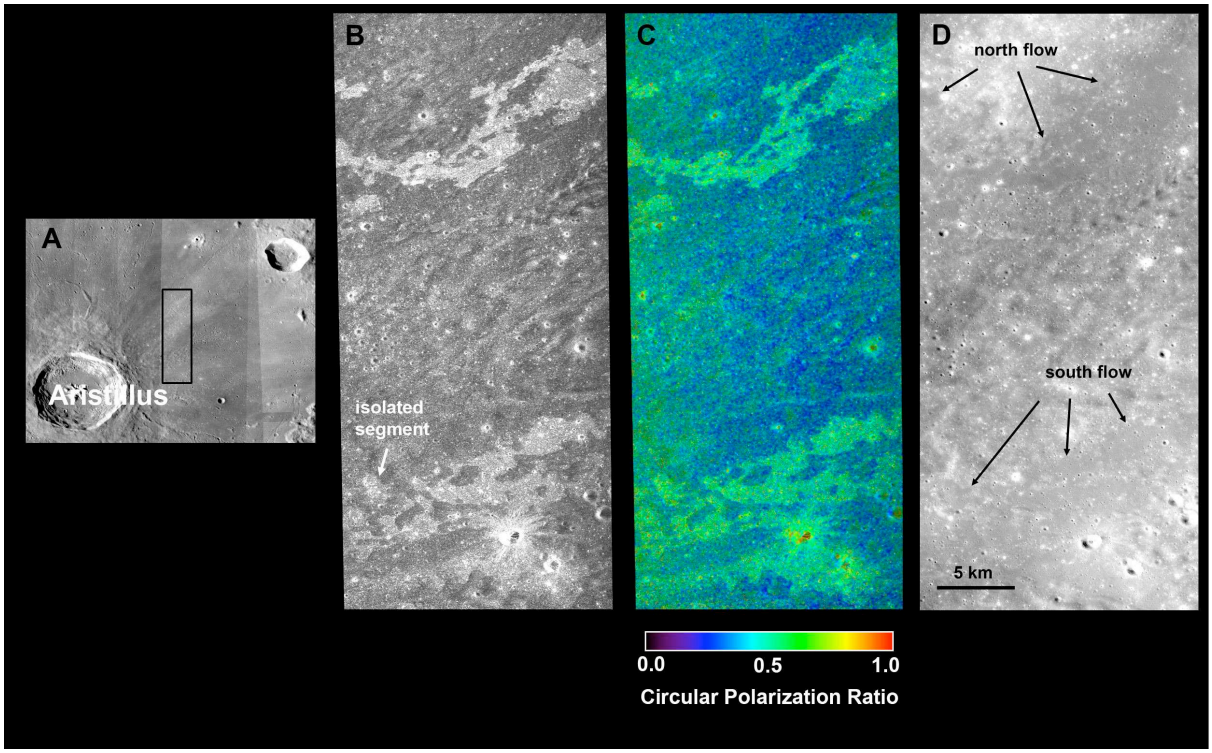

746

747 **Figure 3:** Four images of the impact melt flows northeast of Aristillus. (a) A context image
748 from the LROC WAC mosaic. (b) Mini-RF total power image; radar illumination is from the
749 right. The radar-bright impact melts are mostly connected, but some isolated ponds are
750 present. (c) Mini-RF CPR image, stretched to a color scale and overlaid on the total power
751 image. The impact melts have higher CPR values than the surrounding terrain, but they are
752 less than what is measured for Tycho. The gradient across the image is due to the calibration
753 errors discussed in section 2. (d) Kaguya Terrain Camera image of the same area. The melt
754 flows are barely visible and have been smoothed over by a regolith coating.

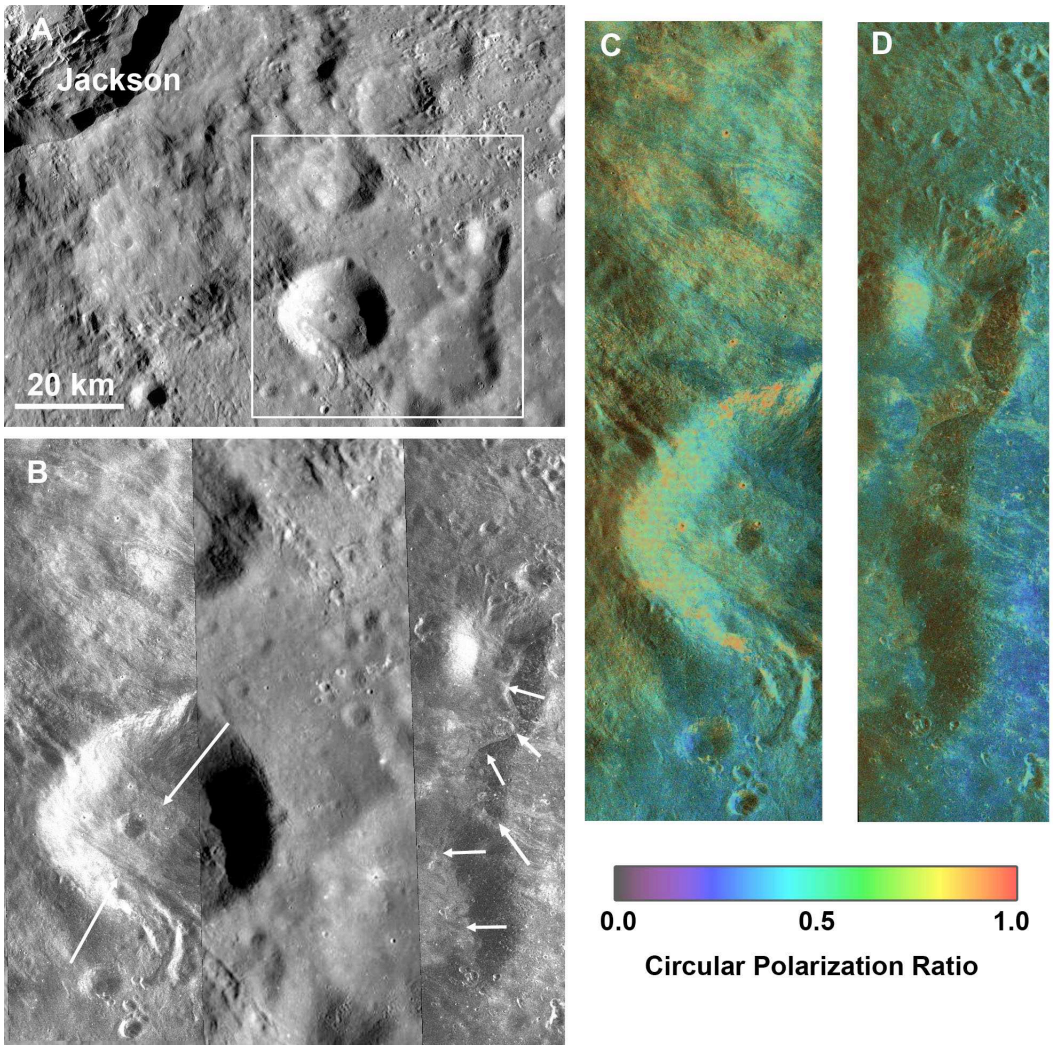

Figure 4: Flow features east of Jackson crater. (a) An LROC WAC context image showing the location of the radar data. (b) Radar total power images (left and right sides) overlaid on the WAC image. Radar illumination is from the right. Arrows mark the positions of flow-like features. Although the features are somewhat brighter than their surroundings, they are not as bright and well-defined as the Tycho and Aristillus melt flows. (c) CPR image of the western (left) radar image in (b), generated by stretching the CPR data to a color scale and overlaying on the total power image. (d) A CPR overlay of the eastern (right) radar image in (b). Parts of the flow features have CPR values that are slightly elevated compared to nearby terrain, but the CPR values are not distinctly different from the proximal ejecta, as is seen at Tycho and Aristillus. Optical images show no evidence of ponded melt. These features may be generated by debris flows.

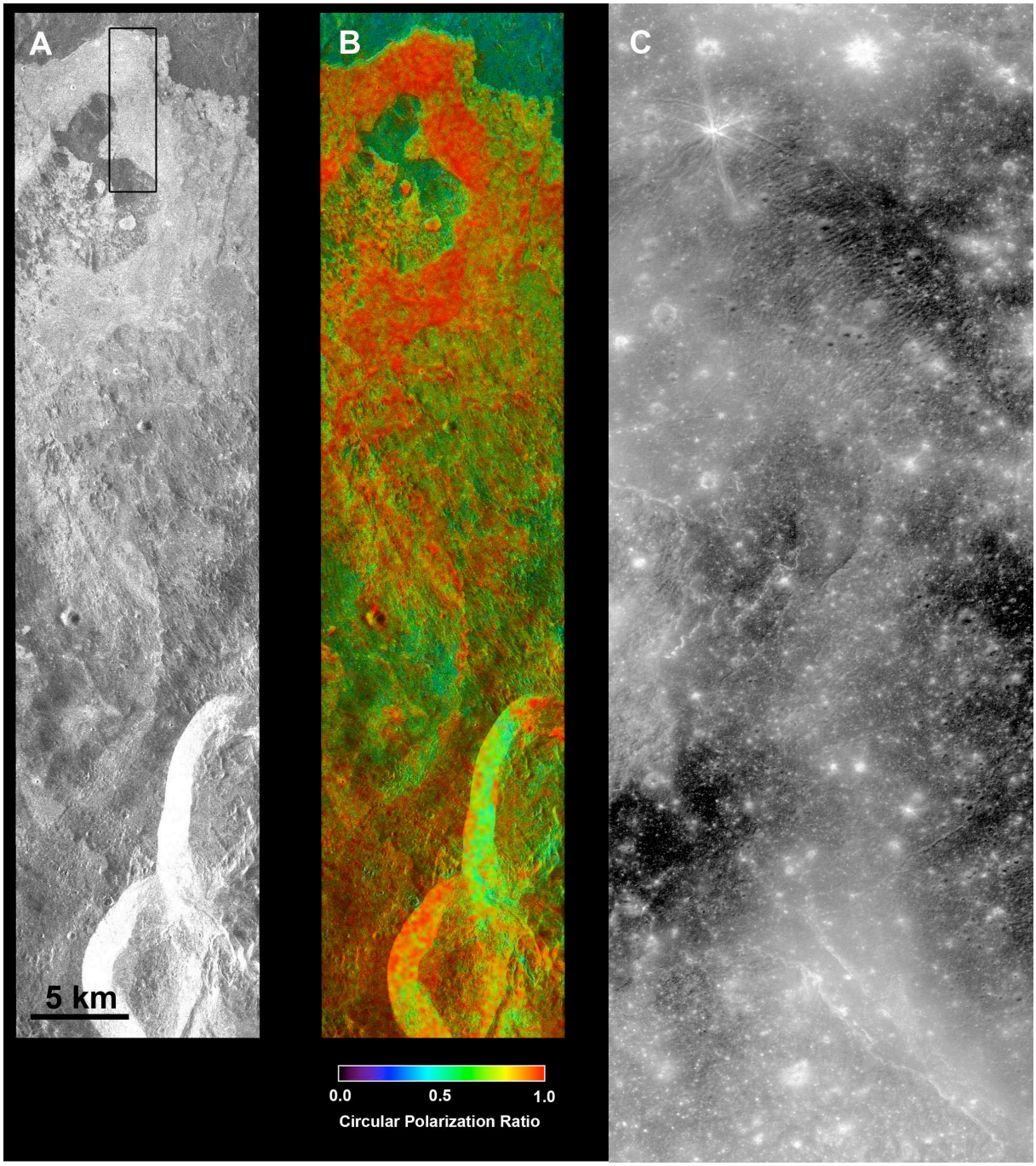

768

769

770 **Figure 5:** Flows north of the crater Glushko. (a) Mini-RF total power image. Radar
771 illumination is from the right. The location of the image in part C is shown with a box. (b)
772 CPR image stretched to a color scale and overlaid on the total power image. (c) An LROC
773 NAC image of part of the Gluskho flows. As with Tycho, radar-bright, high CPR parts of the
774 flow have rugged flow features, such as pressure ridges. The flow features are not pronounced
775 as they are for Tycho, and the surface may have a thicker mantling layer.
776

776

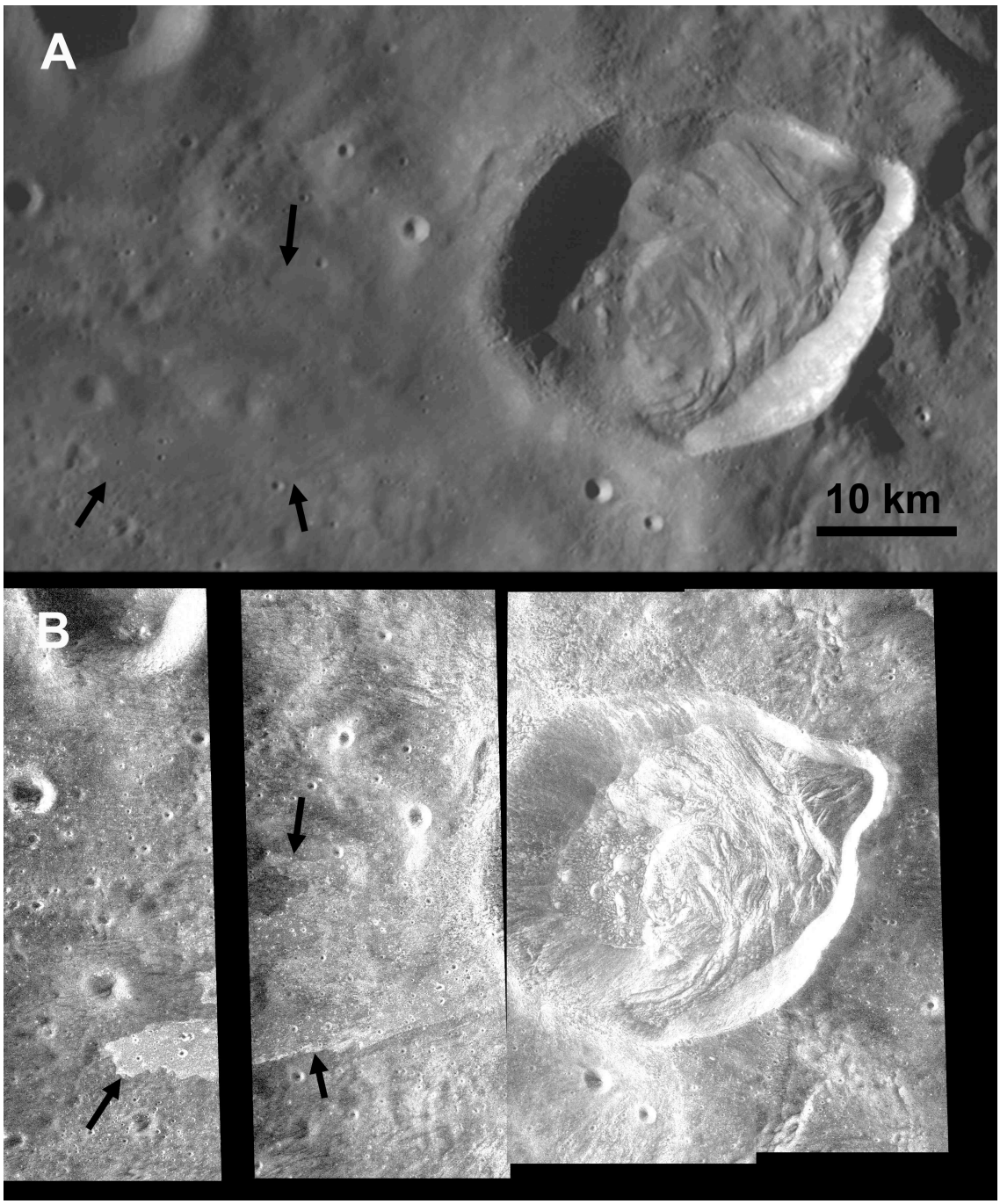

777

778 **Figure 6:** Impact melt flows west of the crater Gerasimovich D. (a) An LROC Wide-Angle
779 Camera image of the crater and surrounding area. The impact melt flows are visible in some
780 places, but are generally covered by regolith. (b) Mini-RF total backscatter power images.
781 Radar illumination is from the left. The radar wave penetrates through thin regolith cover to
782 reveal the flow outlines. The flow has a fairly uniform radar brightness compared to the
783 Tycho and Glushko flows, but there are subtle brightness changes that may indicate smoother
784 and rougher parts of the buried flow or variations in regolith depth.
785

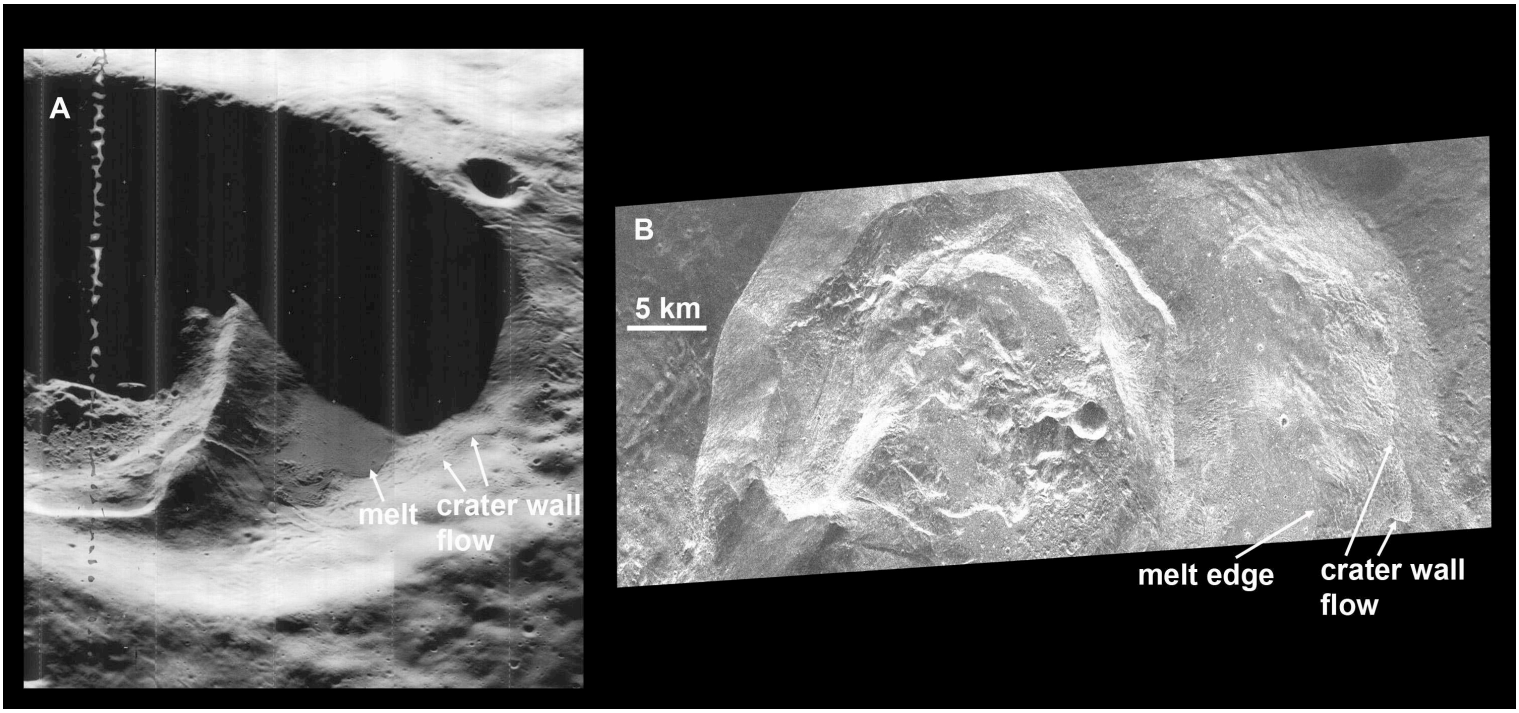

785

786

787 **Figure 7**: The Wiener F flow and pond. (a) High-resolution Lunar Orbiter images (LO5-
788 103H2 and H3) have a lighting geometry that highlights the structure of the melt pond. The
789 pond has rough ridges on the surface. North is to the right in this image. Arrows highlight the
790 same features in both images: the edge of the melt pond and a flow feature higher on the rim.
791 (b) Mini-RF total power image of the pond. North is to the right, and the radar illumination is
792 from the top. The flow feature on the crater wall is particularly apparent in the radar data.
793
794

795

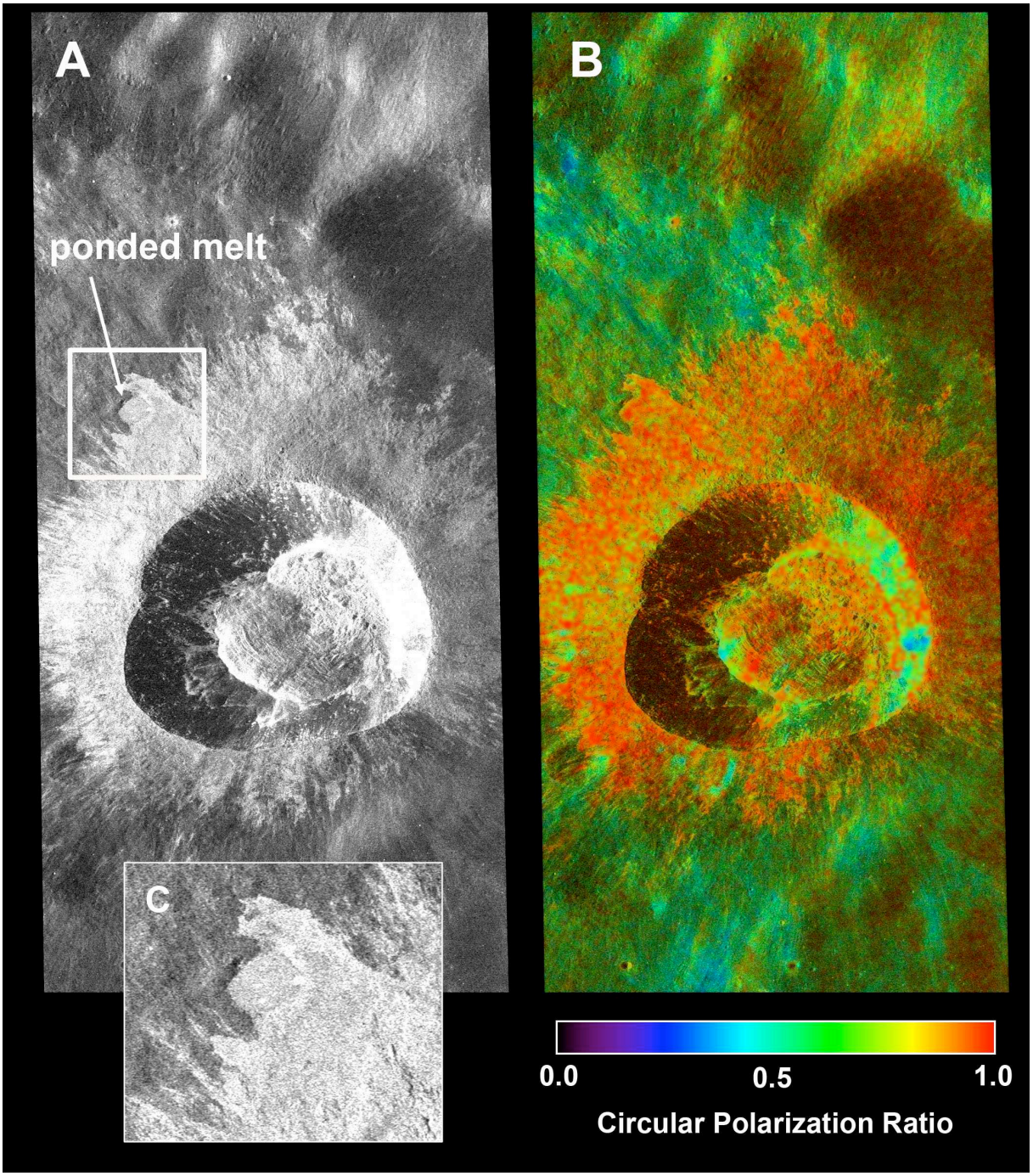

Figure 8: Mini-RF images of a pond associated with a small (13.5 km), unnamed crater (30.9° S, 145.5° E). (a) The total power backscatter radar image. Radar illumination is from the left, and the position of image part C is shown with a box. (b) The circular polarization ratio, stretched to a color scale and overlaid on the total power image. The pond is radar-bright with high CPR values. (c) Total power image of the small pond, which is cratered.

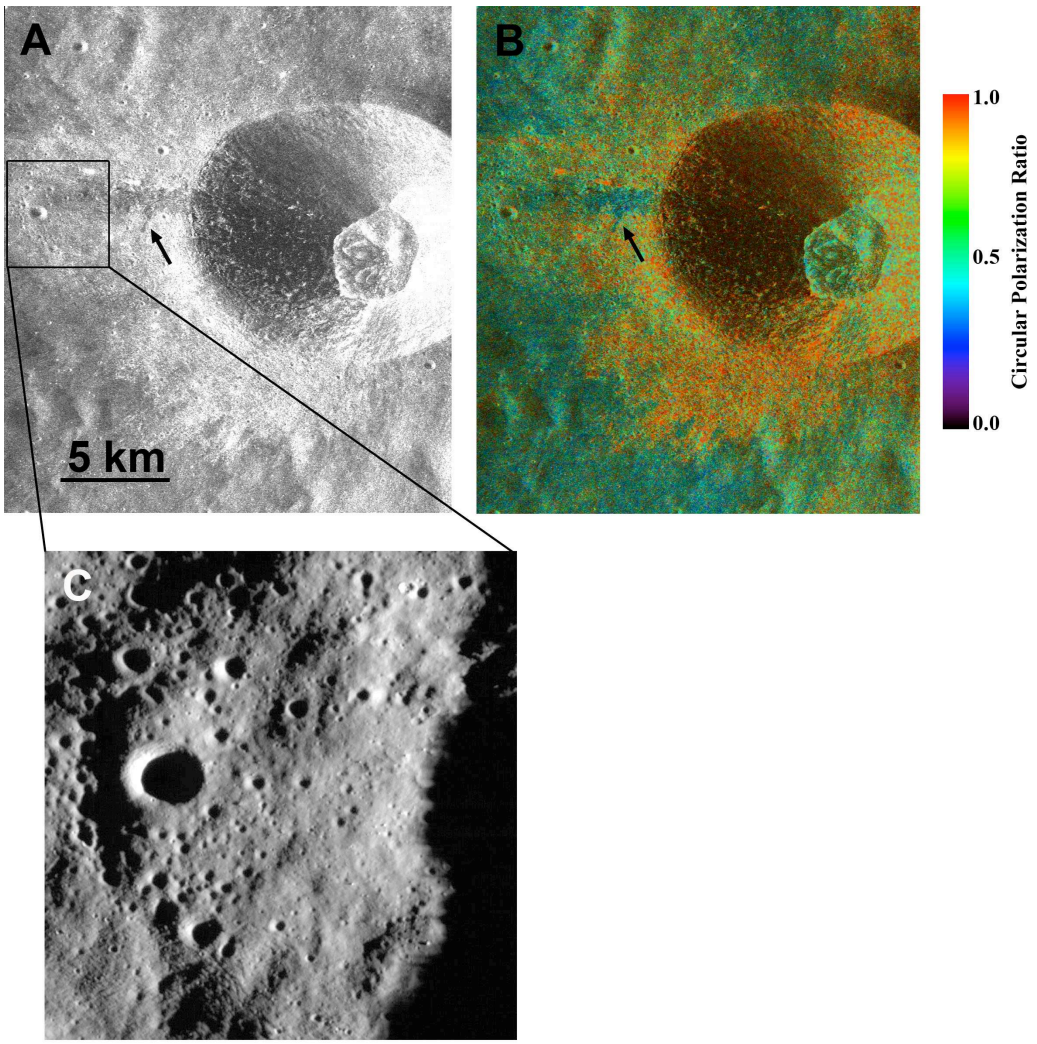

803

804 **Figure 9:** An unnamed 13-km diameter crater (35.7° N, 166.0° E) with an unusual radar-dark
805 lane on top of a possible melt flow or veneer. (a) The radar total power image; illumination is
806 from the left. The location of the Kaguya image in part c is marked with a box. (b) The
807 circular polarization ratio image stretched to a color scale and overlaid on the total power
808 image. (c) A Kaguya image of part of the impact melt and radar-dark region. There is no
809 obvious surface expression of the radar-dark lane. Arrows in (a) and (b) mark the location of a
810 thin outshoot of the dark lane that has rounded edges suggestive of some type of flow.
811

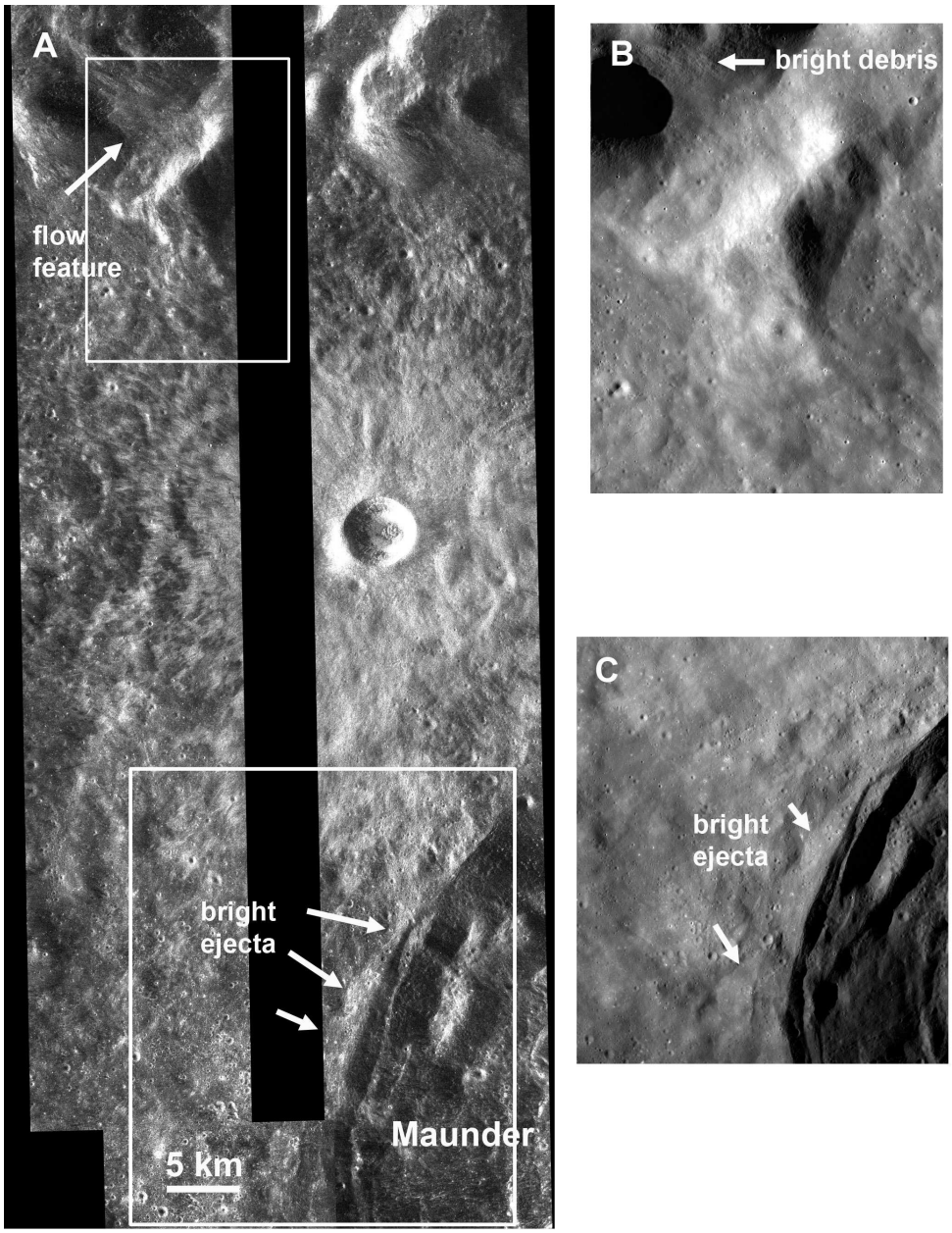

811

812

813 **Figure 10:** Images of flow features associated with a small (5 km diameter) crater northeast
814 of Maunder crater in the Orientale basin. North is towards the top of the images. (a) A radar
815 total-power image mosaic; illumination is from the left. The location of the images in parts b
816 and c are marked with boxes. Arrows mark the location of flow-like features distant from the
817 central crater. (b) A Kaguya Terrain Camera image of a flow feature northwest of the crater.
818 The feature corresponds to an area of bright debris that appears to have flowed downhill into a
819 valley. (c) A Kaguya Terrain Camera image of radar-bright crater ejecta that has been
820 deposited along the rim of Maunder crater.
821
822

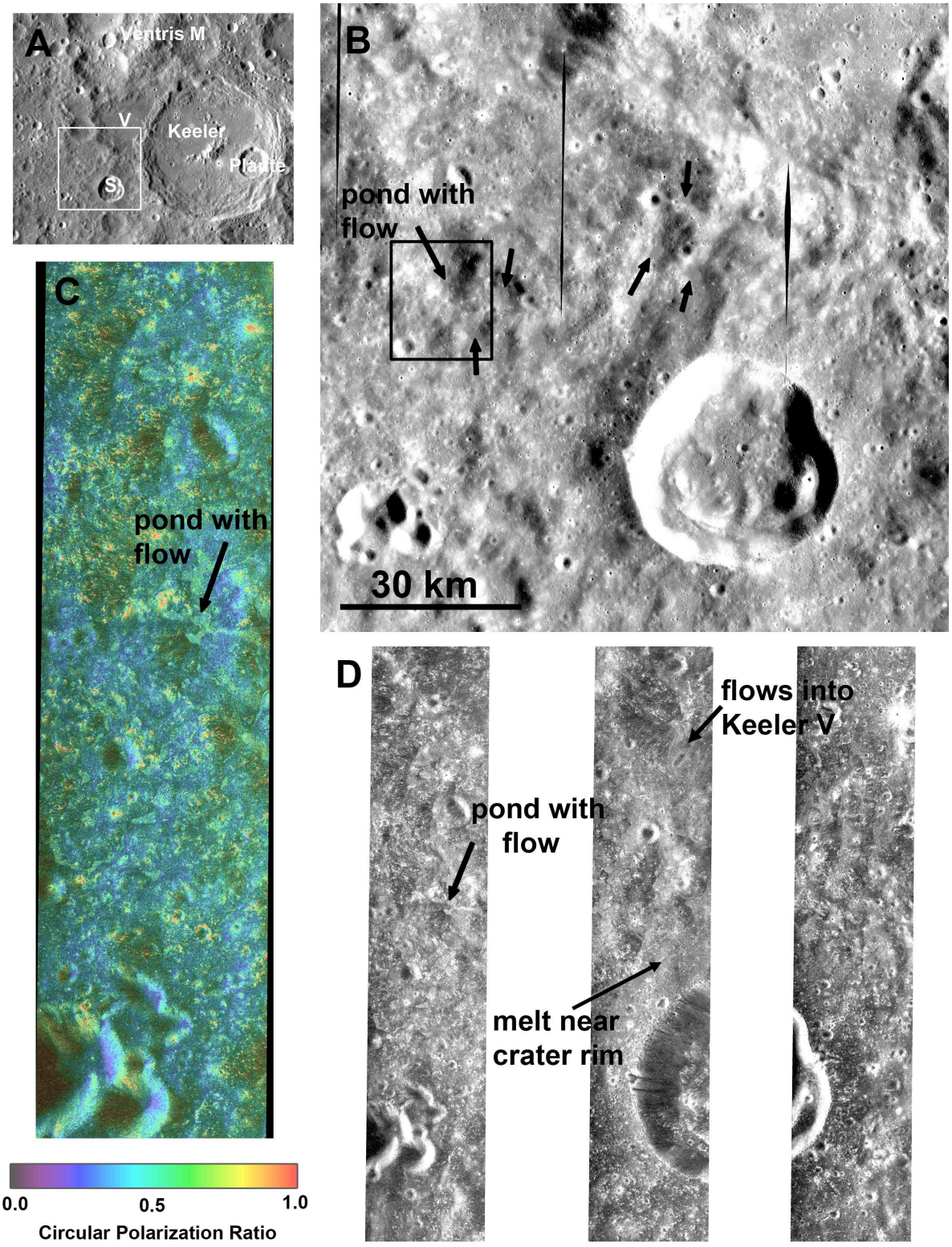

822

823 **Figure 11:** Images of ponds and flows near Keeler crater. Most of the melt is north of the
824 crater Keeler S. (a) A LROC WAC context image with craters labeled. A box marks the
825 locations of parts b and d. (b) A Kaguya Terrain Camera image of the area of ponds. Some of

826 the more easily visible ponds are marked with arrows. An arrow also marks the location of a
827 small pond and flow that is easily visible in the radar data. A box marks the area covered by
828 the close-up images in Figure 12. (c) A circular polarization ratio image of part of the melt
829 pond field. This image corresponds to the left-most radar image in part d. The location of the
830 small pond and flow is marked. Most of the ponds have CPR values between 0.6 and 0.7,
831 suggesting that they are rougher than their surroundings, but probably partially buried. (d)
832 Radar total backscatter images of the area shown in part b. The backscatter images show
833 multiple radar-bright ponds and flow features, including flows into Keeler V. Radar
834 illumination is from the left.
835

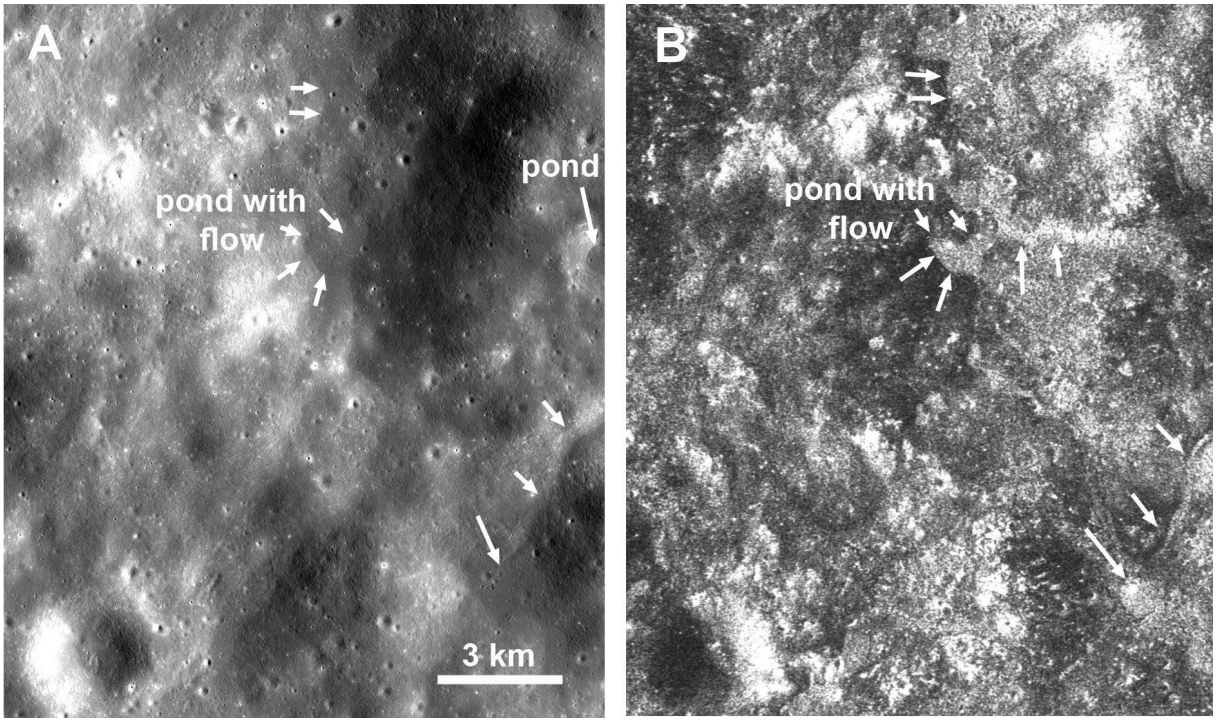

Figure 12: A close-up view of Keeler-area melt ponds and flows. The image location is marked in Figure 11. (a) Kaguya image with ponds marked. (b) Corresponding total power radar image. Note that in the optical image, the illumination is from the right but in the radar image, the illumination is from the left. Arrows mark the position of ponded material at the bottom of a hill. The radar image shows a radar bright streak that could be melt material that flowed down the side of the hill. On the right side of the optical image, there is a pond that does not appear to show up in the radar data, probably because the radar viewing geometry shifts the bottom of the crater off the edge of the image. An additional, barely visible, pond is visible in the lower right of the image. Arrows mark the pond and a slightly flat sinuous ridge leading down to the pond.

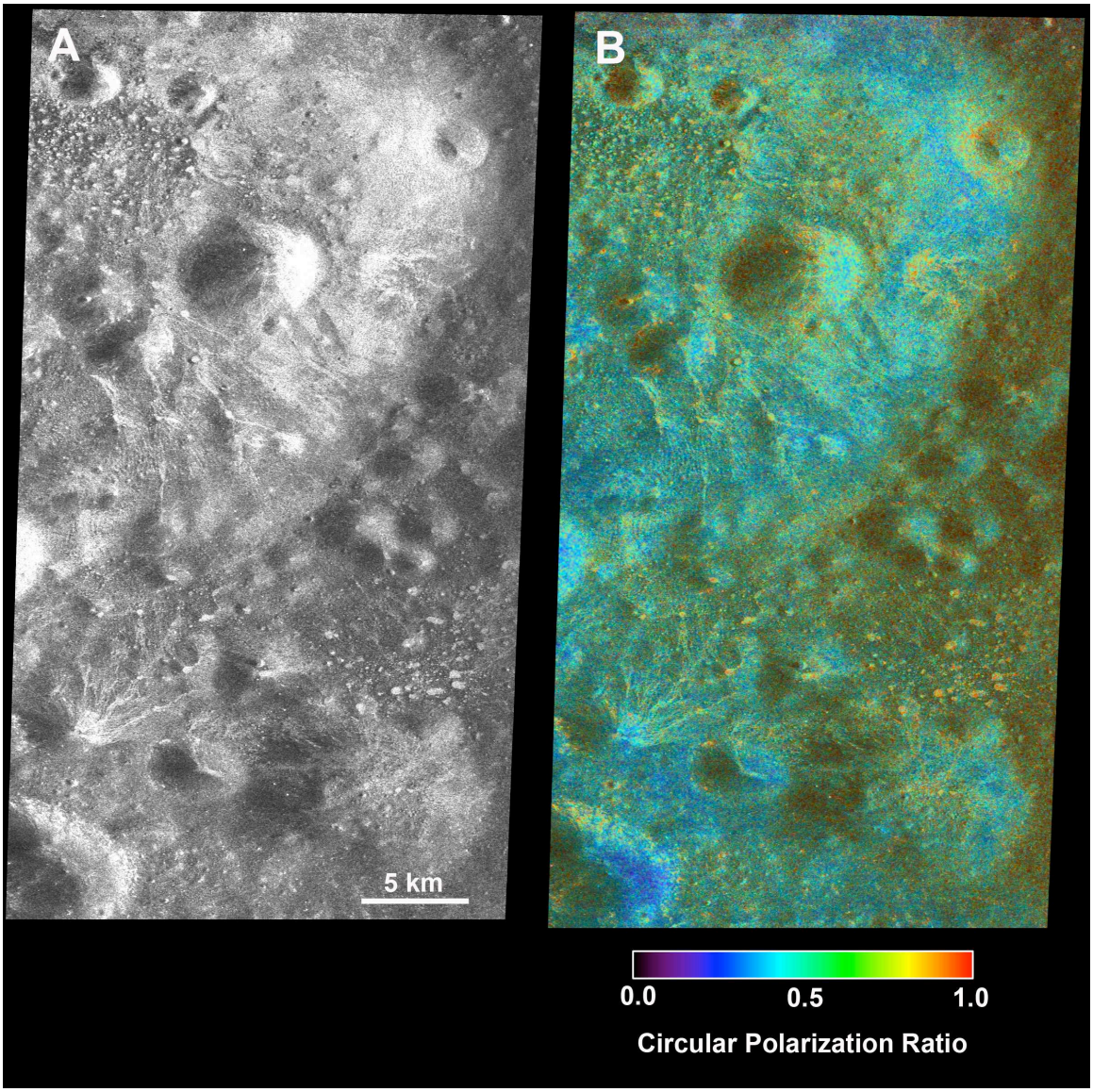

847
848
849 **Figure 13:** Mini-RF images of the pond field located at 41° N and 166° E [*Robinson et al.*
850 2011]. (a) Total backscatter power. (b) Circular polarization ratio image stretched to a color
851 scale and overlaid on the total power image. The ponds at this site have higher CPR values
852 than the ponds at Keeler, but they also appear to be less buried in both radar and optical
853 imagery [*Robinson et al.* 2011]. Radar illumination is from the left.
854

855